Structure evolution in electrorheological fluids flowing through microchannels

Bian Qian, Gareth H. McKinley, and Anette Hosoi*

Received Xth XXXXXXXXXX 20XX, Accepted Xth XXXXXXXXX 20XX
First published on the web Xth XXXXXXXXXX 20XX
DOI: 10.1039/b000000x

Enhanced knowledge of the transient behavior and characteristics of electrorheological (ER) fluids subject to time dependent electric fields carries the potential to advance the design of fast actuated hydraulic devices. In this study, the dynamic response of electrorheological fluid flows in rectilinear microchannels was investigated experimentally. Using high-speed microscopic imaging, the evolution of particle aggregates in ER fluids subjected to temporally stepwise electric fields was visualized. Nonuniform growth of the particle structures in the channel was observed and correlated to field strength and flow rate. Two competing time scales for structure growth were identified. Guided by experimental observations, we develop a phenomenological model to quantitatively describe and predict the evolution of microscale structures and the concomitant induced pressure gradient.

Introduction

Electrorheological (ER) fluids are materials whose rheological characteristics can be altered through the application of an external electric field[1]. Typical ER fluids consist of micron-sized non-conductive or weakly-conductive particles suspended in an insulating fluid. Upon the application of a strong electric field, the particles become polarized and aggregate via electrostatic interactions, into columns aligned along the field direction. The formation of columnar structures induces a dramatic increase in the apparent fluid viscosity, leading to a phase transition in ER fluids from a liquid to a solid-like state. Such transitions occur rapidly and are generally reversible when the electric field is removed. These unique features make ER fluids an ideal class of materials for use in a variety of hydraulic components, including valves[2,3], clutches[4] and shock absorbers[5]. Recently, custom-formulated ER fluids have been employed in a number of microscale applications[6–8] and in various microfluidic devices[9–12]. With the recent discovery of nanoparticle-based ER fluids[13], the expansion of applications to even smaller scale devices can also be envisioned. As a result of this versatility, ER fluids have been of continuing interest to the scientific and engineering communities since their discovery. Over the past few decades, numerous research efforts have been made to enhance our fundamental understanding of these materials and a prominent theme that arises in these studies centers on the question of the dynamic ER material response.

Early rheology measurements show that the stress response of an ER fluid subject to a temporally stepwise electric field is not only dependent on fluid chemistry but also on flow conditions[14]. For ER fluids undergoing steady shear, the characteristic time for the shear stress to reach steady state is proportional to shear rate and only weakly dependent on electric field strength. The shear-rate dependence of the stress response was confirmed in later experiments and an exponential increase in shear stress over time was observed[15,16]. This shear-rate dependence of the stress response was ascribed to a hypothesized rate-dependence associated with column breakup and formation. However, this explanation lacked supporting evidence owing to the technical challenges associated with direct observation of the evolution of particle structures.

Further investigations of the shear response of ER fluids have revealed that the increasing shear stress passes through three sequential stages[17]. In the first stage, the shear stress climbs dramatically; this stage occurs on the scale of several tens of milliseconds. During the second stage, the stress increases more moderately. In the last stage, the increase of shear stress is slow and the growth persists for several seconds. A similar temporal response was observed in the optical response of ER fluids[18–20]; the measured light transmittance of a quiescent ER suspension displayed a significant transmittance enhancement upon the application of electric field. Following the initial enhancement, the transmitted light intensity continuously increased but at a reduced rate, eventually reaching a plateau. Since the variation of light transmittance is a direct result of changes in the microstructure, the corre-

spondence between the stress and optical response of ER fluids suggests a correlation between the stress increase and structure evolution. However, in the absence of direct observation of structure growth under relevant flow conditions, the details of this relationship remain unclear.

Thanks to advances in high speed imaging, real-time visualization of structure formation in ER fluids has recently become feasible. The first such experiments were carried out to observe structure formation in a quiescent ER fluid and measurements correlating particle concentration and field strength were performed[21,22]. A clear dependence of structure formation time on particle concentration and field strength was found. Further investigations revealed that the structure growth – like the evolution of stress – is comprised of three stages[23,24]. In the earliest stage, randomly distributed particles become polarized and aggregate into chains. Subsequently, individual chains coalesce into metastable columns. In the final stage, these metastable columns grow into thicker stable columnar structures. These three stages correspond to the three previously observed periods of stress response and the duration of each stage of structure growth was found to be comparable to the corresponding stages observed in stress measurements. In addition to these experimental observations, a number of simulation studies have been carried out to advance understanding of the rheology and kinetics of structure formation in ER fluids[25–29].

These previous studies, however, concentrated on ER fluids in steady shear (Couette flow) or in a quiescent state. For ER fluids in a pressure-driven flow mode (Poiseuille flow), only a few publications exist, despite the relevance of this flow type in many electrorheological applications such as flow valves and dampers. In contrast to direct measurements of the wall shear stress, pressure drop – which quantifies the driving force required to push fluid through a channel of a prescribed geometry at a given flow rate – is typically measured to characterize the response of ER fluids in flow mode. Previous experiments have shown that the evolution in the pressure drop of ER flows in a channel is a nonlinear function of the time that the electric field has been applied[30]. The transient time to achieve a steady pressure drop was found to depend on field strength, temperature and particle conductivity. To rationalize this transient pressure drop, a Bingham-fluid-based model was recently proposed[31,32]. Computed pressure responses from the proposed model are in good agreements with the experimental measurements, however, the parameters employed in the model cannot be independently determined without additional knowledge of their physical origins.

Further experimental investigations to observe structure growth in ER fluids[33,34] have found that the rate of structure growth and the maximum size of the individual structures are determined by the competition between the field-induced particle interaction force and hydrodynamic forces. Similar dependencies were also observed in flowing magnetorheological fluids[35]. Corresponding pressure measurements indicate that the pressure drop is strongly dependent on field strength, which is in consistent with the results obtained for ER fluids in shear geometries. The field-strength dependence of the pressure response can be rationalized qualitatively from the observed structure growth. However, a quantitative correlation between pressure drop and structure growth has not yet been achieved in these studies. In addition, although spatial variation in the microstructure was briefly mentioned in previous studies[33,34], a systematic investigation of these variations and the resultant effect on the net pressure drop has not been performed.

In the present study, we experimentally investigate the evolution of microstructure in ER fluids under a range of shear rates, between $90\,\mathrm{s}^{-1}$ and $400\,\mathrm{s}^{-1}$. Our study is focused to fluids flowing in rectilinear microchannels and undergoing a temporally stepwise electric field. We aim at understanding the aggregate structure growth across the entire channel and its dependence on flow conditions, rather than the formation of a single column. In addition, the transient pressure drop across the channel is correlated to the structure growth by evaluating the resistance $\frac{\Delta P}{Q}$ from the structure to the fluid flow, a ratio of the pressure drop ΔP to the flow rate Q. We present the pressure data in the form of flow resistant $\frac{\Delta P}{Q}$ because $\frac{\Delta P}{Q}$ can be used conveniently by people in designing channels for valves and dampers (i.e. what ΔP is required for a given Q). Finally, we construct a phenomenological model to complement the experimental observations.

Experimental Methods

A transparent rectangular microchannel was designed and fabricated for our study. Figure 1 shows the configuration of the channel, which consists of three sections: a test section for flow visualization, and two auxiliary sections at the entry and the exit. In the test section, two pieces of $250\,\mu$m thick and 10 mm long copper film were used to form the channel walls, separated by a uniform $250\,\mu$m gap. In the auxiliary sections, the channel walls are made up of non-conductive polyether ether ketone film ($250\,\mu$m thick, 10 mm long) with a separation

Hatsopoulos Microfluids Laboratory, Department of Mechanical Engineering, Massachusetts Institute of Technology, 77 Massachusetts Avenue, Cambridge, Massachusetts 02139. Fax: +1 617-253-8559; Tel: +1 617-253-4337; E-mail: peko@mit.edu

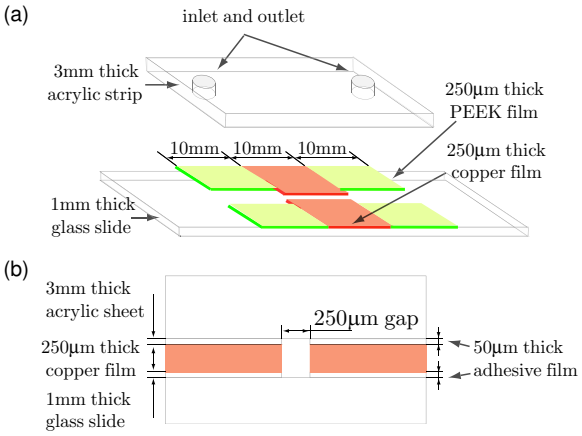

Fig. 1 (a) Schematic of a microchannel fabricated for flow visualization and pressure measurements. (b) Cross-sectional view of the microchannel in the flow direction.

of 3 mm. To form a closed channel, these films were adhered, using a 50 μm thick adhesive film (3M, 966), to a 1 mm thick glass slide and a 3 mm thick acrylic strip serving as a cover sheet. At either end of the flow channel, tapped holes were fabricated in the cover sheet to mount the inlet and the outlet adapter. To apply the electric field within the flow channel, the conductive copper channel walls were connected to a high voltage power supply (Stanford Research PS350) via a driver circuit board. Using external triggers, the electric field can be switched on and off via the driver circuit board and synchronized with measurement devices.

For flow imaging, the microfluidic chip was mounted onto an inverted optical microscope (Nikon TE-2000S). The flow channel was illuminated from above by a collimated light source and viewed with a 2X microscope objective (NA=0.06) from below. A high speed camera (Phantom V5) connected to the microscope was used to record the structure evolution at a frame rate of 400 fps. With these optical arrangements, the depth of field of the imaging system was 240 μm and the image resolution 8.5 μm/pixel.

The ER fluid used in the experiments was a colloidal suspension of polyurethane particles with silicone oil as a carrier fluid (Fluidicon, RheOil4). The mean diameter of the dielectric particles is 2 μm and its volume fraction in the stock solution is $\phi_{\mathrm{f,in}} = 0.41$. For imaging purposes, the stock solution was diluted with 100 cSt silicone oil to $\phi_{\mathrm{f,in}} = 0.02$ in all experiments. The prepared particle solution was injected into the flow channel using a gas-tight glass syringe (Hamilton, 1005TLL) which was connected to the flow channel via stainless steel tubes. To maintain a continuous fluid flow within the channel, a syringe pump (Harvard Apparatus, PHD Ultra) was used to control the flow rate Q in a range of 20-80 μL/min. The shear rate at this flow rate is estimated to be 95-380 s^{-1} from reference[36]. A differential pressure sensor (Honeywell, 26PCBFA6D) with a measurement range of 34.47 kPa was inserted to measure the pressure drop between the entry and the exit of the flow channel. Signals from the pressure sensor were amplified and acquired by a data acquisition card (National Instrument, DAQ1200).

Experimental Results and Discussion

Typical images of the structure evolution in the ER flow within a microchannel are shown in Figure 2. In the absence of an applied electric field, particles disperse uniformly throughout the carrier fluid. Owing to the difference of refractive index between particles and base fluid, the illuminating light is scattered multiple times as it propagates through the particle solution, resulting in a low transmittance of light. Therefore, the image of the flow in the channel appears as a uniform gray ribbon as shown in Figure 2 (top row). By contrast, when an electric field is applied, particles rapidly aggregate into small clusters and columns. As a result of this phase separation, voids and columns are formed, alternating along the channel and resulting in a spatial variation in transmittance of light. At locations of large voids, light is transmitted with little loss and the corresponding regions are bright in the image. In regions where particles are closely packed, most of the illumination light is blocked, resulting in dark shadowed regions. Regularly spaced columnar structures appear as stripes as shown in the lowermost panel of Figure 2.

Following the initial structure formation, the columns initially formed coarsen and new columns form as fresh particle-laden fluid flows into the channel. Continuous coarsening and densification leads to a reduction of porosity and a concomitant decrease in optical transmission across the channel. As the number of columns and the thickness of each individual column increase, the particle density reaches a critical value above which almost all of the illumination light is blocked, leaving a continuous dark region as highlighted in Figure 2. This low-transmittance region first appears near the entry and then expands continuously downstream, indicating a faster structure growth rate in the upstream regions. We attribute this inhomogeneous structure growth to the uneven spatial distribution of flowing particles inside the channel. At the entrance, fresh particles are continuously injected and therefore the volume fraction ϕ_{f} of free (i.e. unstuck) particles is high. As particles flow down the channel, some of them adhere to existing fixed columnar

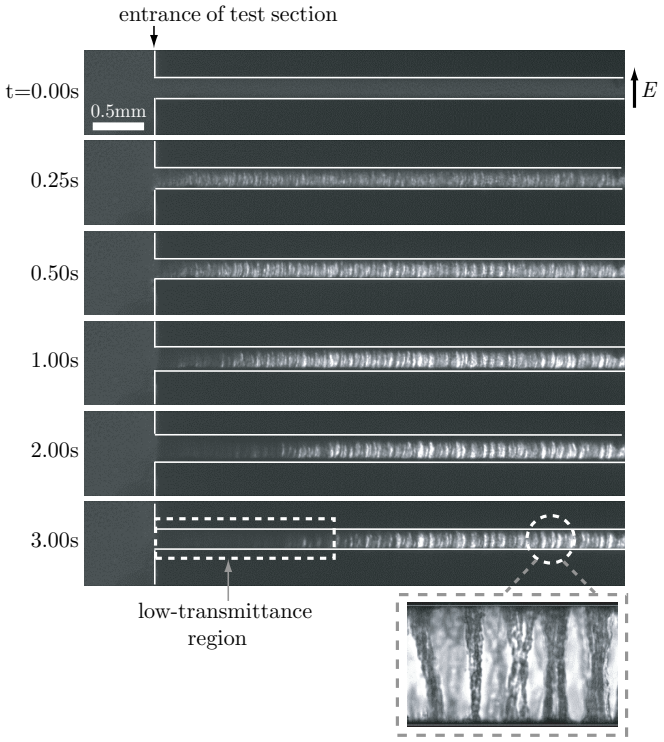

Fig. 2 Images of structure formation and subsequent coarsening during pressure-driven flow of an ER suspension inside a straight microchannel. The channel is 250 μm wide (between the upper and lower electrodes) and 350 μm deep (into the page). The channel walls are indicated with white lines. The particle suspension (2% v/v) flowed from left to right at a constant flow rate of 60 μL/min. An electric field E=4kV/mm was applied perpendicular to the channel walls at $t = 0$. A low-transmittance region which is densely packed with particle columns is highlighted in the final image at the bottom left. The figure insert at the bottom right is a close-up of the loosely spaced particle columns.

structures, resulting in a reduction of number of available free particles downstream. Assuming the rate at which free particles become stuck particles is linearly proportional to the number of available free particles, it follows that the number of flowing particles decreases exponentially with distance x down the channel. Therefore, close to the entrance structures grow more rapidly.

However, the local volume fraction of stuck particles $\phi_s(x)$ cannot grow indefinitely since a minimum porosity must be maintained to allow for continuous fluid flow; as ϕ_s increases, the resistance to fluid flow increases. As a result, the hydrodynamic stress τ_h on the particle columns increases until ϕ_s reaches a critical value, at which the hydrodynamic stresses exert the maximum stress τ_y that the column can withstand. Above this critical value, the column breaks, causing a local reduction of ϕ_s which leads to a new round of column formation. These processes of column breakup and formation result in an average steady state value for ϕ_s at which the local volume fraction of stuck particle achieves a maximum, $\phi_{s,max}$. In regions where $\phi_s(x) = \phi_{s,max}$, no net additional flowing particles are trapped. Instead they move with the fluid flow toward regions of $\phi_s(x) < \phi_{s,max}$, driving the expansion of the low-transmittance region.

The competition of τ_y and τ_h determines the maximum volume fraction $\phi_{s,max}$ of stuck particle. The Mason number[37,38], which is defined by $\mathrm{Mn} = \frac{\tau_y}{\tau_h}$, is used to characterize the relative importance of τ_y to τ_h. We expect the hydrodynamic stress to scale as $\tau_h \sim \mathrm{f}(\phi_s)\frac{\eta Q}{AL}$ where $\mathrm{f}(\phi_s)$ is an increasing function of ϕ_s, A and L are the cross sectional area and the length of flow channel, respectively. In addition, the yield stress $\tau_y(E)$ is expected to increase with field strength E. Since $\phi_{s,max}$ is achieved when $\mathrm{Mn} \sim 1$, $\phi_{s,max} \sim \mathrm{f}^{-1}(\frac{AL}{\eta}\frac{\tau_y(E)}{Q})$. From this scaling, we expect $\phi_{s,max}$ to increase with increasing E and decrease with increasing Q.

To quantify how the field strength E and flow rate Q affect structure growth, experiments were carried out over a range of flow rates and electric fields. To simplify comparison among different tests, a two dimensional intensity map was generated to display the evolution of particle structures, as illustrated in Figure 3(a). The intensity map is an aggregate of the channel center lines shown in Figure 2. Each vertical line on the aggregate map is a snapshot in time. The gray value on the map measures the intensity of the transmitted light and thus it is an indication of the local particle concentration. As the maps show, at the beginning of the image acquisition, no electric field is applied to the channel and the transmitted light intensity is constant along the vertical line (corresponding to the dark region for $t < 0$ in Figure 3). However, when the electric field is applied at $t = 0$, parti-

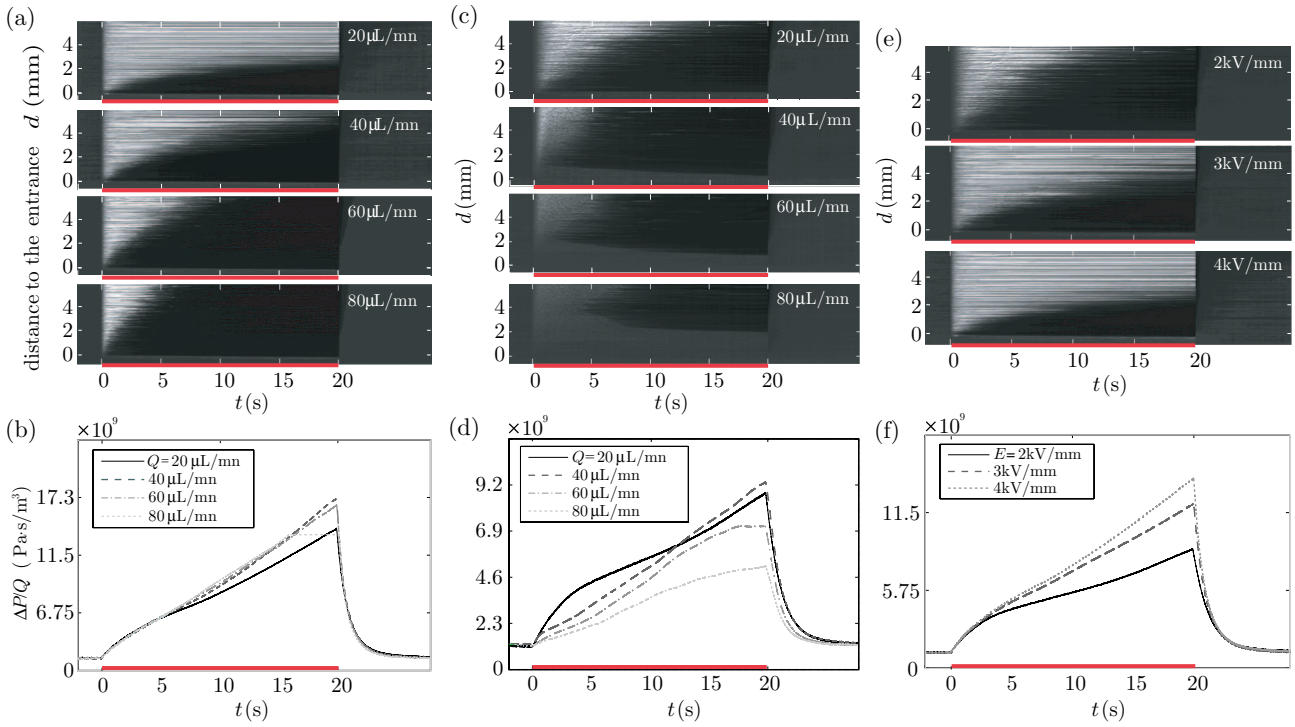

Fig. 3 (a) Intensity maps displaying structure evolution in a microchannel with an applied electric field of E=4 kV/mm. Each vertical line on the map is an extraction of the image pixels along the center line of the flow channel from the experimental images as shown in figure 2. The map represents the temporal evolution of transmitted light and the temporal change of number of particles aggregates along the channel. Maps are shown for four different flow rates, 20, 40, 60 and 80 μL/min. The red line on each plot indicates the states of electric field (red = on). (c) Intensity maps for flows with a relatively low electric field E = 2 kV/mm. (e) Intensity maps at a constant flow rate, Q = 20 μL/min, with varying electric field strengths. (b)(d)(f) Measurements of flow resistance $\frac{\Delta P}{Q}$ corresponding to (a), (c) and (e), respectively.

cles begin to aggregate and columns form. Fixed particle columns appear as a thin horizontal gray lines on the intensity maps. Subsequent to the initial column formation, more and more particles accumulate at the entry, indicated by a growing region of high particle concentration and low transmittance. On the intensity map, the lower black segment of each vertical line corresponds to an instantaneous image of the growing low-transmittance particle-rich region. The edge of the dark region on the intensity map represents the front of the growing low-transmittance region. After the electric field is switched off, the particle columns are progressively washed out and the channel refills with evenly dispersed moving particles with volume fraction $\phi_f = 0.02$ (as indicated by the uniform dark gray area at late times).

Using the generated intensity maps, we first compare the structure growth at different flow rates with a fixed electric field strength E=4 kV/mm. As shown in figure 3(a), all intensity maps show similar features when the electric field is applied. At the initial stage, loosely spaced columns build up along the entire channel. Subsequently a low-transmittance region forms around the entry and grows along the flow direction. However, the rate of growth of the low-transmittance region is observed to vary with the fluid flow rate Q: the higher the flow rate the faster the low-transmittance region expands. The change in expansion rate is partly attributed to the variation in the rate at which particles are delivered at the inlet. At high flow rates more particles flow into the channel per unit time, increasing the rate of particle delivery and accelerating the structure growth. If $\phi_{s,max}$ is independent of flow rate, it follows that the flow resistance $\frac{\Delta P}{Q}$ builds up more rapidly with increasing flow rate. Measurements of $\frac{\Delta P}{Q}$ (figure 3(b)) indeed show a more rapid increase in $\frac{\Delta P}{Q}$ when Q is increased from 20 to 40 μL/min. However, further increase of flow rate from 40 μL/min to 60 μL/min and to 80 μL/min does not promote additional change in flow resistance, suggesting that $\phi_{s,max}$ is itself a function of flow rate Q. As discussed previously, $\phi_{s,max}$ is expected to decrease with increasing Q. Therefore, $\frac{\Delta P}{Q}$ might not grow with further increase in Q since $\frac{\Delta P}{Q}$ is not only determined by the total number of particles flowing into the channel but also by the spatial distribution of particles.

Following measurements at high electric fields, we performed a series of experiments at relatively low fields in which the flows exhibit markedly different behavior. As shown in figure 3(c), no stripes are present on the intensity maps except at the lowest flow rate, indicating that no fixed particle columns built up along the channel. Although particles still aggregate into small clusters when the electric field is applied and the flow resistance increases, the interactions between these particle clusters and the channel walls are not strong enough to resist hydrodynamic stresses and form stationary columns spanning the channel. Instead the particle clusters move with the fluid flow, leading to random temporal variations in local light transmittance. Although no fixed structures form, particle aggregation still enhances light transmittance, resulting in a lighter average gray intensity. This transmittance enhancement becomes weaker as flow rate increases, indicating a slow and relatively weak clustering process at high flow rates. At late stages, even at these low fields and high flow rates, some particle clusters may grow sufficiently large, occasionally leading to a fixed particle column that forms across the channel. Once this column nucleates, more and more particle columns form. Correspondingly, on the intensity map, a dark spot emerges at some distance away from the entry and grows both toward the entrance and the exit. The formation of the first fixed column appears to be random and the subsequent growth of the particle dense region is difficult to predict quantitatively. However, a general trend is observed for the first appearance of the fixed column: as flow rate increases, the fixed column appears at a location further away from the entry and at later times. This observation suggests that the higher the flow rate, the smaller the probability of building a full-length column that spans the channel.

Corresponding flow resistance measurements across the channel reveal that the first formation of fixed particle chains is critical to the initial growth of flow resistance. As shown in figure 3(d), the flow resistance builds up fastest at the lowest flow rate. As flow rate increases, flow resistance grows more slowly until fixed chains start building in the channel. This retarded growth of flow resistance with increasing flow rate is in contrast to the enhanced growth in flow resistance at high electric fields.

Comparisons were also performed for flows under different electric fields as shown in figure 3(e). At a low flow rate Q=20 μL/min, fixed columns build along the entire channel upon application of the electric field. Following this initial formation, column coarsening and densification progresses. As before, a particle dense region forms near the entry and expanded. It is seen from the maps that under a lower electric field the front of the low-transmittance region propagates at a higher speed. This observation indicates a higher $\phi_{s,max}$ in the low-transmittance region as field strength increases since the rate at which particles flow into the channel is the same for all three tests. Note that although a stronger electric field leads to faster particle aggregation, the speed of structure growth is less dependent on the strength of

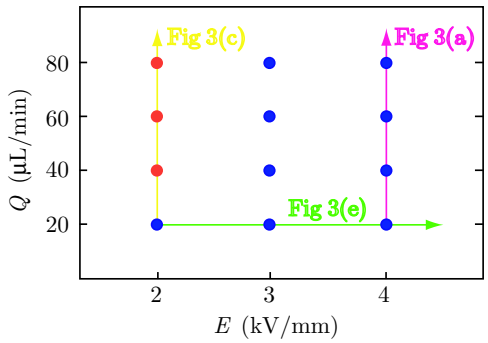

Fig. 4 A schematic diagram illustrating the different regimes of structure growth. Dots represent experimental tests at different settings of Q and E. Colors are used to indicate the types of structure growth: limited by column stability (red) and limited by particle delivery (blue). Typical intensity maps are shown in Fig. 3 for displaying structure growth.

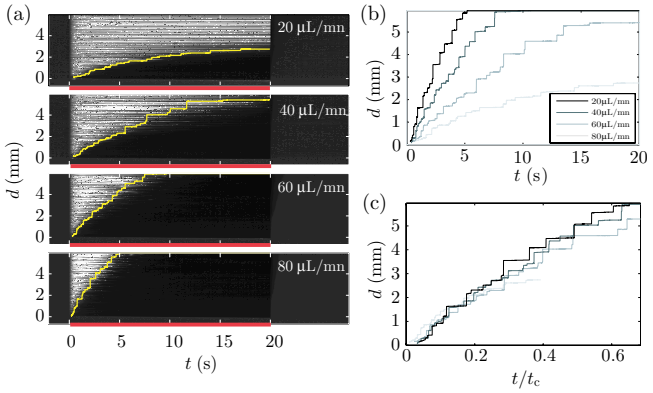

Fig. 5 Expansion of low-transmittance regions at different flow rates. (a) Extracted moving fronts (yellow lines) of the low-transmittance regions plotted on top of the respective the intensity maps. (b) Front movements obtained in (a) for different flow rates. (c) Scaled front movements.

electric field, and rather is limited primarily by the rate of particle delivery.

In accordance with the measured structure growth, the flow resistance built up rapidly under all tested electric fields. At early stages, the growth of flow resistance is almost indistinguishable between different fields. However, at late stages, a faster growth rate is observed in $\frac{\Delta P}{Q}$ under higher electric fields. This observation reveals that the flow resistance is not only determined by the total number of particles stuck in the channel but also determined by the spatial distribution of the stuck particles.

Two modes of structure growth are thus identified: limited by chain stability and limited by particle delivery. For the first one, the hydrodynamic stress is initially high and particle interaction is week. Therefore, particle chains easily break under hydrodynamic stress and stationary chains seldom form across the channel. Microchannel flows operating at high Q under low E fall into this category. For the second one, hydrodynamic stress is initially low compared to the inter-particle stress. When the electric field is applied, columns spanning over the gap between electrodes form immediately. As free particles are recruited from the incoming flow, columns grow continuously. Since the time for initial column formation is short, the speed of structure growth is limited by particle delivery. Such a mode of structure growth is observed in flows operating at low Q with high E. A schematic diagram shown in figure 4 illustrates the different regimes of structure growth.

In addition to qualitative descriptions, we quantitatively measure the expansion rate of the low-transmittance region by extracting the front position from the intensity map. The front evolution curves presented in figure 5(a) are obtained by first converting the intensity map to a binary image using thresholding and then tracing the boundary of the largest connected cluster on the converted binary map. The threshold value for image conversion is selected to be the mean gray intensity of the flow image under $E = 0\,\mathrm{kV/mm}$. The extracted front locations for different Q are plotted in figure 5(b). All front evolution curves display a quasi-linear increase at short times. The slope of the curve increases with flow rate. Since the slope measures the expansion speed of the low-transmittance region, it can be expressed as $\frac{Q\phi_{\mathrm{f,in}}}{A(\phi_{\mathrm{s,max}}-\phi_{\mathrm{f,in}})}$ in which Q is the fluid flow rate, A the cross-sectional area of the flow channel, $\phi_{\mathrm{f,in}}$ the volume fraction of free particles in the fluid in the absence of electric fields and $\phi_{\mathrm{s,max}}$ the maximum volume fraction of stuck particles in the channel. With the average measured slopes and the prescribed experimental parameters Q, $\phi_{\mathrm{f,in}}$ and A, $\phi_{\mathrm{s,max}}$= 0.45, 0.36, 0.31 and 0.27 can be obtained for corresponding flow rates Q=20, 40, 60 and 80 μL/min, respectively. The decrease of $\phi_{\mathrm{s,max}}$ with increasing Q is in agreement with our initial expectation. Using the estimated $\phi_{\mathrm{s,max}}$, we define a characteristic time $t_{\mathrm{c}} = \frac{AL(\phi_{\mathrm{s,max}}-\phi_{\mathrm{f,in}})}{Q\phi_{\mathrm{f,in}}}$ which characterizes the time scale to fill the channel with particles that are delivered by the incoming fluid stream. By normalizing time t with the defined t_{c}, all front evolution curves collapse on to a single curve as shown in figure 5(c).

Model

The experimental observations described above are markedly different from anything that could be simulated

with a continuum model, e.g. Bingham flow in a channel[31,34,39,40]. The Bingham fluid model is commonly used to describe the macroscopic plastic behaviors of ER suspensions and it is useful for predicting the steady pressure drop of ER flows in a channel. However, the Bingham fluid model is not itself amenable to description via a microscopic view of suspension structure. Therefore, it does not allow one to capture any structure evolution along the channel and hence precisely predict the transient pressure drop across the channel.

Guided by the experimental observations, we construct a simple model for describing the evolution of particle structures and the accompanied change of flow resistance. Since the size of a particle and the radius of a particle column are both small compared to the length of the flow channel, we take a continuum approach to model particle distribution. With this assumption, the volume fraction of stuck particles $\phi_{\rm s}(x,t)$ and the volume fraction of free particles $\phi_{\rm f}(x,t)$ can be approximated as a continuous function of time t and distance from the entrance x. Note that $\phi_{\rm s}$ is computed relative to the volume of channel slice $A{\rm d}x$ while $\phi_{\rm f}$ is defined relative to the volume of fluid within this slice, $A(1-\phi_{\rm s}){\rm d}x$. With these definitions of $\phi_{\rm f}$ and $\phi_{\rm s}$, conservation of particles can be expressed as

$$\frac{\partial \phi_{\rm f}(1-\phi_{\rm s})}{\partial t} + u(1-\phi_{\rm s})\frac{\partial \phi_{\rm f}}{\partial x} + \frac{{\rm d}\phi_{\rm s}}{{\rm d}t} = 0, \qquad (1)$$

in which $u(x,t)$ is the average local flow speed. For a constant flow rate, u can be related to $\phi_{\rm s}$ by $u = \frac{Q}{A(1-\phi_{\rm s})}$. 1D plug flow is assumed in the model so that u is constant across the cross section perpendicular to the channel axis. The first term in equation 1 represents the rate of change of the number of free particles. The second term describes the change of free particles due to flow convection. The final term denotes the rate of change from free particles into stuck particles. To get a closed-form solution for equation 1, an expression for $\frac{{\rm d}\phi_{\rm s}}{{\rm d}t}$ is required. Since the particle dense region exhibits a quasi-linear expansion at short times, we assume that the growth of stuck particles $\frac{{\rm d}\phi_{\rm s}}{{\rm d}t}$ is linearly proportional to the number of free particles in the fluid phase, $\alpha\phi_{\rm f}(1-\phi_{\rm s})$. The proportionality constant α represents the probability for a free particle become incorporated into the structure per unit time and it is a measurement of the time scale for particle aggregation α^{-1}. For simplicity, α is assumed to be constant for fixed E. Given this, an equation for the volume fraction growth of stuck particles can be written as

$$\frac{{\rm d}\phi_{\rm s}}{{\rm d}t} = \alpha(E)\phi_{\rm f}(1-\phi_{\rm s})\{1-{\rm erf}[\frac{Q}{MA}-\mathcal{P}(E)]\}, \qquad (2)$$

in which the growth of $\phi_{\rm s}$ is cutoff with an error function. The argument of the error function $\frac{Q}{MA}-\mathcal{P}(E)$ is a comparison between the hydrodynamic stress on the particle structures and the holding stress of particle columns. The maximum pressure gradient which the particle structures can sustain is given by $\mathcal{P}$. Since $\mathcal{P}$ measures the strength of particle-particle attraction, it is primarily determined by the strength of the applied electric field E. Growth in the number of stuck particles is arrested when this maximum pressure gradient is comparable to the local pressure drop $\frac{Q}{M(x,t)A}$ where $M(x,t)$ is the flow mobility. Flow mobility is a monotonically decreasing function of $\phi_{\rm s}$. The error function defines a maximum fraction of stuck particles $\phi_{\rm s,max}$ above which $\frac{Q}{MA}-\mathcal{P}(E)$ becomes positive and the growth of $\phi_{\rm s}$ stops.

To relate the local flow mobility $M(x,t)$ to $\phi_{\rm s}(x,t)$, the particle columns are assumed to be an array of cylinders in a hexagonal packing arrangement. With this approximation, the flow mobility can be calculated using the analytical expression obtained in[41],

$$M = M_1\xi_1 + M_2\xi_2, \qquad (3)$$

in which

$$M_1 = \frac{1}{3\sqrt{3}}\frac{r^2}{\eta}\frac{(1-l^2)^2}{l}\left[\frac{3{\rm arctan}\sqrt{(1+l)/(1-l)}}{\sqrt{1-l^2}} + \frac{l^2}{2}+1\right]^{-1}, \qquad (4)$$

and

$$M_2 = \frac{r^2l^2}{4\eta}(\frac{\frac{1}{8}l^{-4}-s}{s^2})^{-1}. \qquad (5)$$

Here $l = \frac{2\sqrt{3}}{\pi}\phi_{\rm s}$, $s = {\rm ln}l - \frac{3}{4} + l^2 - \frac{1}{4}l^{-4}$, η is the fluid viscosity and r is the radius of the particle column. The mobility coefficients M_1 and M_2 represent the flow mobility obtained for high and low $\phi_{\rm s}$, respectively. They are only valid for $\phi_{\rm s}$ at the extreme ends. To calculate M over a wide range of $\phi_{\rm s}$, equation 1 was constructed by asymptotically matching M_1 and M_2 at the extreme ends using the weighted functions of $\xi_1 = 1-{\rm e}^{\beta[1/\phi_{\rm s}+1]}$ and $\xi_2 = 1-{\rm e}^{\beta[-1/(1-\phi_{\rm s})+1]}$. The constant $\beta = 0.8$ was chosen from literature[41].

Note that the flow mobility predicted by equations 3-5 is not only dependent on $\phi_{\rm s}$ but also dependent on the radius of the particle columns r. In the experiments, r varies over time due to column coarsening. However, for simplicity, r is set to be constant in the calculation, a valid approximation provided the growth of stuck particles primarily increases the number of columns rather than thickening existing particle structures. Since r and $\mathcal{P}$ are unknown from experiments, they were adjusted to match the calculations to the experimental measurements. With the calculated $M(x,t)$, flow resistance $\frac{\Delta P(t)}{Q}$ can be evaluated by $\int_0^L \frac{1}{M(x,t)A}{\rm d}x$.

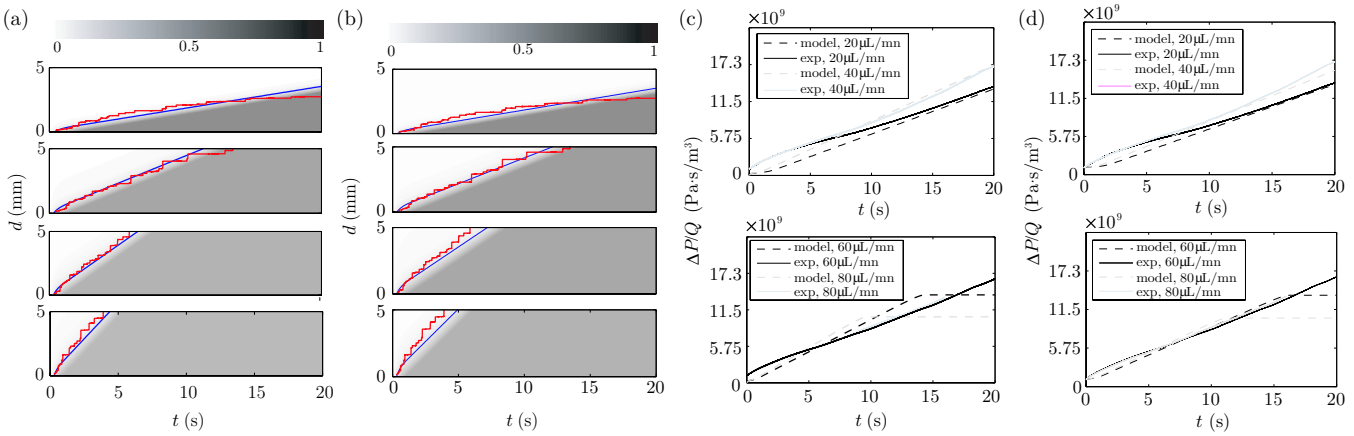

Fig. 6 Comparisons of front positions and flow resistance between experiments and calculations. (a) Contour plots of the calculated $\phi_s(x,t)$ for varying flow rates, Q=20, 40, 60 and 80 μL/min, from top to bottom. Equation 3 is used to compute the mobility M in the calculations. The gray value at each point represents the value of ϕ_s, as indicated by the gray scale bar on the top. Red curves indicate experimentally measured front positions from figure 5. Blue curves are lines of $\phi_s = 0.1$. (b) Calculated $\phi_s(x,t)$ using equation 6. (c)(d) Calculated flow resistance $\Delta P/Q$ (dashed) in comparison with the measured resistance for different flow rates. (c)(d) correspond to (a)(b), respectively. The plateau of the dashed line in the bottom panels indicates a steady state of $\frac{\Delta P}{Q}$ at which $\phi_{s,max}$ in the entire channel.

In addition to equation 3, a simpler expression, which asymptotically captures the low and high ϕ_s flow mobility limits exactly, was used for comparison:

$$M = (1-\phi_s)^n M_0. \tag{6}$$

Here M_0 is the mobility of a flow in an empty channel $\phi_s = 0$. Given the channel dimensions and the fluid viscosity, $M_0 = 3.03\times10^{-8}\,\frac{m^2}{Pa\cdot s}$ can be determined analytically for a rectilinear channel. The constant n is fit to the data.

To solve equations 1-2, appropriate initial and boundary conditions are needed for ϕ_s, ϕ_f. To reproduce experiments, $\phi_f(x,0) = \phi_f(0,t) = \phi_{f,in} = 0.02$ and $\phi_s(x,0) = 0$ for all calculations. In addition, a constant flow rate constraint was enforced in the calculation. The model equations were solved numerically using an upwinded scheme to approximate the spatial derivatives and integrating the resulting ordinary differential equations with a forth order Runge-Kutta method.

Numerical Results

The calculated evolution in $\phi_s(t)$ are presented in figure 6(a)(b). Parameter values $r = 33\,\mu$m, $\mathcal{P} = 6$ MPa/m, α=10 s^{-1} and $n = 6.2$ were chosen for all calculations. The column radius r used in calculations is about twice larger than the experimental one which is measured from the images of the visible columns. Considering only the columns in the region $\phi_s(x) \ll \phi_{s,max}$ are visible, we expect larger column radius in the particle dense region $\phi_s(x) = \phi_{s,max}$ since coarsening process progresses as $\phi_s(x) < \phi_{s,max}$. Note that τ_h is related to $\mathcal{P}$ by $\mathcal{P}hw \cong 2\tau_h(h+w)$, in which h and w are the width and the height of the channel[36]. With the fitting parameter $\mathcal{P}$, we get an estimation on the yield stress $\tau_y \sim \tau_h \sim 438$ Pa. The evaluated τ_y is about half of the one, $\tau_y = 1000$ kPa, obtained from steady shear measurement for an undiluted fluid (41% v/v) operating at $E = 4$ kV/mm. The discrepancy in τ_y might be attributed to the change of particle volume fraction since the volume fraction of stuck particle $\phi_{s,max}$ in the flow channel might be lower than the one of an undiluted fluid used in the shear measurement. Moreover, the measurements in different geometries, Poiseuille flow and Couette flow, might lead to a different τ_y, which has been reported in previous experiments[42]. As the contour maps show in figure 6(a)(b), the calculated ϕ_s using Eqn. 3 and Eqn. 6 are almost identical. In agreement with the experimental observation, a particle-dense region ($\phi_s(x) = \phi_{s,max}$) originating at the entrance continuously expands toward the exit. Under the same electric field E=4 kV/mm, the expansion rate increases with flow rate, as seen in experiments. Since the relationship of light transmittance with ϕ_s is unknown, it is challenging to extract the front movements from the contour map of $\phi_s(x,t)$ and directly compare them to the ones measured from experiment. To extract the front movements from model calculations, we define the front as the locations where $\phi_s(x)$ reaches at

a critical value. With this definition, the front motions can be traced from model calculation by finding the contour line of ϕ_s on the plot of $\phi_s(x,t)$. We found that the lines of ϕ_s=0.1 best fit with the front movements from experimental measurements as shown in figure 6(a)(b).

Figure 6(c)(d) also shows the calculated flow resistance $\frac{\Delta P}{Q}$ with a direct comparison to the experimental measurements. As the number of stuck particles increases, the calculated flow resistance increases over time. Using either Eqn. 3 or Eqn. 6 for computing M, the calculated flow resistances (dashed lines) are quantitatively comparable to the measured ones (solid lines) in principle for all flow rates. However, it is also seen that calculations predict a slower initial growth of $\frac{\Delta P}{Q}$ relative to those measured in experiments. A potential reason for the slow initial rises in calculated $\frac{\Delta P}{Q}$ is that the resistance to fluid flow that arises from particle migration towards walls have not been included in our simple model. In the experiments, when the field is initially applied particles are dragged perpendicular to the flow direction at the onset of particle chaining. This leads to a significant disruption to the primary flow and hence a large added flow resistance. In addition to these secondary flows, the change of column radius r during initial column formation provides another possible explanation. According to equation 4-5, the flow mobility M scales quadratically with r for constant ϕ_s. At the initial phase of column formation, thin particle chains (one particle wide) first form upon the application of electric field and then chains merge into thicker columns. This integration process results an increase of r and thus a slowed growth in $\frac{\Delta P}{Q}$ at the late stage.

In addition to the discrepancy in initial growth, the calculated $\frac{\Delta P}{Q}$ plateaus to a steady state sooner than the experimental data (bottom plots of figure 6(c)-(d)). At this steady state, the rate at which particles are attracted to the fixed structures is equal to the one at which particle are sheared off from the structures, and an equilibrium is established between particle attaching and detaching. It is clear that the time to reach this steady state is determined by the expansion rate of the low-transmittance region. When the front of the low-transmittance region arrives at the exit, $\phi_s(x) = \phi_{s,max}$ in the entire channel and no more change in $\frac{\Delta P}{Q}$ is expected. The calculations predict a steady $\frac{\Delta P}{Q}$ around t=18 s and 15 s for $Q = 60$ and 80 μL/min respectively (dashed lines). However, the steady $\frac{\Delta P}{Q}$ is not achieved in experiments (solid lines) within the time duration of 20 s. The postponement of the steady $\frac{\Delta P}{Q}$ in the experiment indicates that in the low-transmittance region ($\phi_s(x) = \phi_{s,max}$) ϕ_s is still growing but at a relatively slow rate (i.e. the growth rate α in equation 2 is small but not zero) so that the expansion of low-transmittance region slows. This decelerated growth in ϕ_s suggests a dependence of α on ϕ_s, which we have not captured in our simple model.

Conclusion

We have designed a microfluidic channel with conductive channel walls that enables direct microscopic imaging of a pressure-driven ER fluid flow. With this capability we have visualized the structure evolution in a dilute ER fluid for varying flow rates Q and field strengths E. Quantitative measurement of the structure growth has been made and related to the change of flow resistance using models of flow in porous media.

For a given flow rate Q and field strength E, there exists a maximum volume fraction of particles $\phi_{s,max}$ incorporated into the fibrillar structure that develops in the matrix for structure growth. When $\phi_{s,max}$, an equilibrium is established between the rate of column formation and destruction. The value of $\phi_{s,max}$ can be determined by balancing the hydrodynamic stress which exerts on the column with the yielding stress which the column can hold, Mn $\sim$ 1. For exact prediction of $\phi_{s,max}$, exact models for calculations of hydrodynamic stress and yielding stress are required.

The time to achieve the value $\phi_{s,max}$ in the entire channel is determined by two time scales. One is the time for particle polarization and aggregation $t_a = \alpha^{-1}$. Another is the convection time for sufficient particles to be delivered $t_a = \frac{AL(\phi_{s,max}-\phi_{f,in})}{Q\phi_{f,in}}$. The ratio of $\frac{t_a}{t_c}$ defines a dimensionless quantity which determines the limiting rate of structure growth and hence the time for achieving the maximum $\frac{\Delta P}{Q}$. t_a is typically small ($\sim$100 ms) under electric fields of $E = 3 - 4$ kV. In contrast, t_c can be very small or large, depending on the values of Q, L and $\phi_{f,in}$. For fixed Q and L, t_c is much larger than t_a at low $\phi_{f,in}$. So the structure growth is limited by the rate of particle delivery and the time for achieving steady flow resistance is solely determined by t_c. As $\phi_{f,in}$ increase, t_c reduces. When $\phi_{f,in} \geq \phi_{s,max}$, t_c is negligible and the structure growth is dominated by particle aggregation. For fast actuated hydraulic devices, achieving the best performance (i.e. maximum $\frac{\Delta P}{Q}$) at short times is desired and therefore the use of high volume fraction suspension is preferable.

A phenomenological model has been built for predicting the growth of the particle structure in the channel and the evolution in the flow resistance. By adjusting two unknown parameters, calculation using this one dimensional model reproduces the principle experimental

observations of structure growth and predicts an increase of flow resistance. Although the calculated flow resistance is quantitatively comparable to experimental measurement, an earlier approach to the steady state for $\frac{\Delta P}{Q}$ is predicted by the model. In addition, there is some discrepancy observed in the initial rise of flow resistance when the porous media is very sparse. These differences reveal the complexity of the coupled interactions between particles, fluid flow and electric field, and indicate that exact models for describing these interactions are needed for precise prediction of structure growth.

Although the analysis performed in the study is for microchannel flows operating at constant flow rate, the phenomenological model can be easily adapted for flows operating at constant pressure, by changing the boundary condition at the entry. With the modified model, the performance of a realistic ER valve can be simulated with given system parameters.

Acknowledgments

We would like to thank Ahmed Helal and Maria Telleria for the rheological measurements of yield stress, and Marc Strauss and Mike Murphy for the construction of high voltage driver circuit. This work was supported by DARPA M3.

References

1 W. M. Winslow, *J. Appl. Phys.*, 1949, **20**, 1137–1140.
2 M. Whittle, R. Firoozian and W. A. Bullough, *J. Intell. Mater. Syst. Struct.*, 1994, **5**, 105–111.
3 S. B. Choi, C. C. Cheong, J. M. Jung and Y. T. Choi, *Mechatronics*, 1997, **7**, 37–52.
4 D. Carlson and T. G. Duclos, *Proc. 2nd Int. Conf. on ER Fluids*, 1990, 353–367.
5 S. B. Choi, Y. M. Han, H. J. Song, J. W. Sohn and H. J. Choi, *J. Intell. Mater. Syst. Struct.*, 2007, **18**, 1169–1174.
6 T. Tateishi, K. Shimada, N. Yoshihara, J. W. Yan and T. Kuriyagawa, *Adv. Mater. Res.*, 2009, **69-70**, 148–152.
7 L. Wang, M. Zhang, J. Li, X. Gong and W. Wen, *J. Micro/Nanolith. MEMS MOEMS*, 2009, **8**, 021103.
8 L. Wang, M. Zhang, J. Li, X. Gong and W. Wen, *Lab Chip*, 2010, **10**, 2869–2874.
9 K. Yoshida, M. Kikuchi, J. H. Park and S. Yokota, *Sens. and Actuator A: Phys.*, 2002, **95**, 227–233.
10 X. Niu, W. Wen and Y. K. Lee, *Appl. Phys. Lett.*, 2005, **87**, 243501.
11 L. Liu, X. Chen, X. Niu, W. Wen and P. Sheng, *Appl. Phys. Lett.*, 2006, **89**, 083505.
12 L. Liu, X. Niu, W. Wen and P. Sheng, *Appl. Phys. Lett.*, 2006, **88**, 173505.
13 W. Wen, X. Huang, S. Yang, K. Lu and P. Sheng, *Nat. Mater.*, 2003, **2**, 727–730.
14 J. M. Ginder and S. L. Ceccio, *J. Rheol.*, 1995, **39**, 211–234.
15 Y. Tian, Y. Meng and S. Wen, *J. Intell. Mater. Syst. Struct.*, 2004, **15**, 621–626.
16 Y. Tian, C. Li, M. Zhang, Y. Meng and S. Wen, *J. Colloid Interface Sci.*, 2005, **288**, 290–297.
17 K. Tanaka, A. Sahashi and R. Akiyama, *Phys. Rev. E*, 1995, **52**, R3325.
18 K. L. Smith and G. G. Fuller, *J. Colloid Interface Sci.*, 1993, **155**, 183–190.
19 J. M. Ginder, *Phys. Rev. E*, 1993, **47**, 3418–3429.
20 K. Tanaka, K. Nakamura and R. Akiyama, *Phys. Rev. E*, 2000, **62**, 5378–5382.
21 J. C. Hill and T. H. V. Steenkiste, *J. Appl. Phys.*, 1991, **70**, 1207–1211.
22 D. Klingenberg, C. Zukoski and J. C. Hill, *J. Appl. Phys.*, 1992, **73**, 4644–4648.
23 W. Wen, D. W. Zheng and K. N. Tu, *Appl. Phys. Lett.*, 1998, **85**, 530–533.
24 W. Wen, D. W. Zheng and K. N. Tu, *Rev. Sci. Intrum.*, 1998, **69**, 3573–3576.
25 D. Klingenberg and C. Zukoski, *Langmuir*, 1990, **6**, 15–24.
26 H. See and M. Doi, *J. Rheol.*, 1992, **26**, 1143–1163.
27 R. Tao and Q. Jiang, *Phys. Rev. Lett.*, 1994, **73**, 205–208.
28 R. Tao, *Chem. Eng. Sci.*, 2006, **61**, 2186–2190.
29 G. Bossis, C. Métayer and A. Zubarev, *Phys. Rev. E*, 2007, **76**, 041401.
30 S. Ulrich, G. Böhme and R. Burns, *J. of Phys.: conf. Ser.*, 2009, **149**, 012031.
31 Y. M. Han, Q. H. Nguyen and S. B. Choi, *Smart Mater. Struct.*, 2009, **18**, 085005.
32 Y. S. Jeon, Y. M. Han, Q. H. Nguyen and S. B. Choi, *J. of Phys.: Conf. Ser.*, 2009, **149**, 012012.
33 E. J. Rhee, M. K. Park, R. Yamane and S. Oshima, *Exp. Fluids*, 2003, **34**, 316–323.
34 Y. J. Nam, M. K. Park and R. Yamane, *Exp. Fluids*, 2008, **44**, 915–926.
35 M. Ocalan and G. H. McKinley, *J. Intell. Mater. Syst. Struct.*, 2011, **0**, 1–10.
36 Y. Son, *Polymer*, 2007, **48**, 632–637.
37 P. A. Arp and S. G. Mason, *Colloid Polym. Sci.*, 1977, **255**, 566–1165.
38 A. P. Gast and C. F. Zukoski, *Adv. Colloid Interface Sci.*, 1989, **30**, 153–202.
39 H. G. Lee, S. B. Choi, S.S.Han and J. Kim, *Int. J. Mod. Phys. B*, 2001, **15**, 1017–1024.
40 Y. T. Choi and N. M. Wereley, *J. Intell. Mater. Syst. Struct.*, 2002, **13**, 443–450.
41 M. V. Bruschke and S. G. Advani, *J. Rheol.*, 1993, **37**, 479–498.
42 H. G. Lee and S. B. Choi, *Mater. Design*, 2002, **23**, 69–76.